

Structure Sensitivity of Pd Facets for Enhanced Electrochemical Nitrate Reduction to Ammonia

Jeonghoon Lim, Chun-Yen Liu, Jinho Park, Yu-Hsuan Liu, Thomas P. Senftle,* Seung Woo Lee,* and Marta C. Hatzell*



Cite This: *ACS Catal.* 2021, 11, 7568–7577



Read Online

ACCESS |



Metrics & More

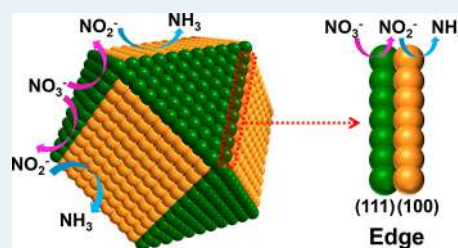


Article Recommendations



Supporting Information

ABSTRACT: The design of electrocatalysts capable of selectively reducing nitrate to ammonia is gaining interest as a means of transforming waste into fertilizers. However, most prior investigations of prototypical electrocatalysts, such as polycrystalline Pd and Pt, have focused on unraveling the mechanisms responsible for the selective reduction of nitrate to nitrogen gas. Such polycrystalline noble metals demonstrate notoriously low activity for nitrate reduction (nitrate to nitrite) and high activity for nitrite reduction (nitrite to nitrogen). Here, we aim to elucidate the effect Pd surface structure has on nitrate and nitrite reduction and to determine what role catalyst structural design can play in enabling selective reduction of nitrate to ammonia. Through synthesizing nanocatalysts with controlled facets (e.g., nanocubes, cuboctahedrons, octahedrons, and concave nanocubes), we demonstrate that Pd(111) > Pd(100) > Pd(*hk*0) for nitrate reduction activity and Pd(100) > Pd(*hk*0) > Pd(111) for nitrite reduction activity in an alkaline electrolyte. Octahedrons without Pd (100) facets exhibited nearly selective production of NO₂[−] with little to no measurable NH₃ or N₂. However, nanocubes that expose only the Pd(100) facet exhibited high activity for NO₂[−] reduction to NH₃. Cuboctahedrons that expose both Pd(111) and Pd(100) facets demonstrated the highest production of ammonia (306.8 μg h^{−1} mg_{Pd}^{−1}) with a faradaic efficiency of 35%. Density functional theory (DFT) simulations reveal that *NO₃ dissociation to *NO₂ + O* is more favorable on Pd(111) than Pd(100), explaining the faster nitrate reduction kinetics on the Pd(111) facet observed in the experiments. The simulations also show that *NO₂ binds less strongly to Pd(111) compared to Pd(100). Thus, nitrite formed via nitrate dissociation readily desorbs from the Pd(111) surface, which explains why Pd(111) selectively reduces nitrate to nitrite. The results show that cuboctahedron is bifunctional in nature, with the (111) facet catalyzing the conversion of NO₃[−] to NO₂[−] and the (100) facet catalyzing the conversion of NO₂[−] to NH₃.



KEYWORDS: nitrate reduction, nitrite reduction, Pd shape-controlled electrocatalysts, selectivity, structure sensitivity, ammonia

INTRODUCTION

Increasing use of nitrogen-based fertilizers is largely responsible for nitrate being one of the most common groundwater contaminants.^{1–3} The significant health concerns attributed to nitrate in drinking water (infant methemoglobinemia and cancer) promote a need for nitrate treatment technologies to meet maximum contaminant guidelines (i.e., <10 ppm) as defined by the US Environmental Protection Agency. Most nitrate removal technologies require the use of physicochemical treatment processes, such as reverse osmosis, ion exchange resins, and electrodialysis. All three approaches result in a significant amount of waste brine that is difficult and expensive to dispose.^{4–6} Catalytic approaches which transform nitrate into less harmful (nitrogen) or useful (ammonia) products are of emerging interest to minimize waste and close the nitrogen cycle.⁷

Electrocatalytic transformations have many potential advantages over thermocatalytic approaches, with the most notable being the ease of integration with renewable electricity. The chief challenge with identifying an ideal electrocatalyst is finding a catalyst that contains active sites for both nitrate

reduction (NO₃RR) and nitrite reduction (NO₂RR), as nitrite is a well-known intermediate present in the catalytic transformation to either nitrogen or ammonia. The NO₃RR activity on noble metals decreases in the following order Rh > Ru > Ir > Pd–Pt.^{4,8–11} The low activity of Pd for NO₃RR is due to the low enthalpy of NO₃[−] adsorption on Pd when compared to hydrogen.^{12,13} Despite the low activity for NO₃RR, polycrystalline Pd expresses the ideal activity for NO₂RR and generates N₂ with high selectivity.^{14–16} Pd also experiences a lower degree of catalyst poisoning when compared with nonprecious metal alternatives, which is critical for long-term performance in complex solutions (wastewater).^{8,12,17,18}

Thus, it is important to investigate the role of Pd catalyst structure in an effort to overcome these tradeoffs and design

Received: March 28, 2021

Revised: May 27, 2021

Published: June 9, 2021



efficient electrocatalysts capable of converting nitrate to ammonia. Most design strategies to overcome slow NO₃RR kinetics on Pd center on the design of bimetallic catalyst on a reducible support. The bimetallic catalyst typically contains Pd and a promoter metal such as In, Rh, Cu, Ni, and Sn.^{4,8,13,17,19–24} With a bimetallic catalyst, the transition metal promotes the reduction of nitrate to nitrite while oxidizing the support. The noble metal then allows for activation of hydrogen, reduction of the support, and further reduction of nitrite to *NO and/or *N₂O. The choice of bimetallic and catalyst structure can promote the favorable accumulation of *NO or *N₂O on the catalyst surface. Spectroscopy investigations have indicated that surfaces that preferentially form *N₂O are critical to producing N₂,^{25–27} while surfaces that preferentially form *NO may be critical to producing NH₃.

Understanding electrocatalytic behavior on precious metals with diverse facets for NO₃RR/NO₂RR is necessary for developing rational design strategies for efficient ammonia production from wastewater. Preferential crystal planes of Pt show a strong structure sensitivity for NO₃RR activity.^{28–39} Koper and co-workers have detailed the structure-sensitive nature of nitrate reduction on Pt catalysts.^{28,40} However, similar investigations regarding the structure sensitivity of Pd using shape-controlled nanoparticles are rare,^{41,42} and thus, our chief aim is to elucidate the nitrate reduction reaction structure sensitivity on Pd. To investigate this, we synthesize Pd shape-controlled nanoparticles to explore the facet-dependent activity and selectivity of NO₃RR and NO₂RR. We find that Pd(111) facets catalyze NO₃[–] to NO₂[–] and Pd(100) facets catalyze NO₂[–] to NH₃.

■ EXPERIMENTAL SECTION

Materials and Methods. *Materials.* Palladium(II) sodium chloride (Na₂PdCl₄, 98%), poly(vinylpyrrolidone) (PVP, MW 55 000), potassium bromide (KBr, ≥99%), L-ascorbic acid (C₆H₈O₆, 99%), formaldehyde solution (HCHO, 37 wt % in H₂O), sodium nitrate (NaNO₃, ≥99%), sodium nitrite (NaNO₂, ≥99%), *p*-aminobenzenesulfonamide (C₆H₈N₂O₂S, ≥98%), *N*-(1-Naphthyl) ethylenediamine dihydrochloride (C₁₂H₁₄N₂, ≥98%), sodium nitroferricyanide(III) dihydrate (C₅FeN₆Na₂O·2H₂O, ≥99%), phosphoric acid (H₃PO₄, ≥85%), sodium hydroxide (NaOH, ≥97%), sodium hypochlorite solution (NaClO, 10–15%), sodium citrate dihydrate (C₆H₅Na₃O₇·2H₂O, ≥99.0%), and salicylic acid (C₇H₆O₃, ≥99%) were all obtained from Sigma-Aldrich. Vulcan XC72R carbon powder used as a support came from Cabot Corporation. The Nafion 212 membrane and commercial Pd/C (20 wt %, 3–5 nm Pd NP) catalyst used in this study were purchased from Fuel Cell Store Company. A nitrate kit (Nitrate TNTplus Vial Test) for nitrate measurements was obtained from HACH Company. Ultrapure water (18.2 MΩ cm) was used from Millipore Milli-Q. All gases were obtained from Airgas.

Synthesis of Pd Nanocubes. Pd nanocubes were synthesized through a previously reported protocol with minor modifications.⁴³ In a typical synthesis,^{44,45} 58 mg of Na₂PdCl₄, 105 mg of PVP, 400 mg of KBr, and 60 mg of L-ascorbic acid (AA) were used as a Pd precursor, a surfactant, a capping agent, and a reducing agent, respectively. PVP, KBr, and AA dissolved in DI water (8 mL) followed by preheated at 85 °C for 15 min under magnetic stirring. The aqueous Na₂PdCl₄ solution (3 mL) was then rapidly injected into the preheated

solution. The reaction solution was kept at 85 °C for 3 h under magnetic stirring and then cooled down to room temperature. The product nanocubes were collected by centrifugation and washed with water and ethanol.

Synthesis of Pd Cuboctahedrons and Octahedrons. Pd cuboctahedrons and octahedrons were synthesized through a previously reported protocol.⁴⁶ In a seed growth synthesis, 0.6 mg of Pd nanocube, 105 mg of PVP, and 0.1 mL of HCHO were used as a seed, surfactant, oxidizing agent, and reducing agent, respectively. The above chemicals were dissolved in ultrapure water (8 mL) in an oil bath to preheat the mixture at 60 °C for 10 min. Each Pd precursor (8.7 mg of Na₂PdCl₄ for cuboctahedrons and 29 mg of Na₂PdCl₄ for octahedrons) is dissolved in each aqueous solution (11 mL) and then placed in an oil bath to heat the mixture at 60 °C for 3 h under magnetic stirring and then cooled down to room temperature. The final steps are precipitation using ethanol and washing by ultrapure water through centrifugation.

Synthesis of Pd Concave Nanocubes. Pd concave nanocubes were synthesized through a previously reported protocol.⁴⁶ In a seed growth synthesis, 0.6 mg of Pd nanocube, 14.5 mg of Na₂PdCl₄, 105 mg of PVP, 300 mg of KBr, and 60 mg of AA were used as a seed, Pd precursor, surfactant, capping agent, and reducing agent, respectively. All chemicals are in an aqueous solution (11 mL) and then placed in an oil bath to heat the mixture at 60 °C for 2 h under magnetic stirring and then cooled down to room temperature. The final steps are precipitation and washing using ethanol and ultrapure water through centrifugation.

Deposition of Shaped-Controlled Pd Nanoparticles on Carbon Support. Shape-controlled Pd nanoparticles were deposited onto Vulcan carbon XC72R by sonication for 3 h in ethanol to obtain carbon-supported catalysts (denoted as Pd nanocube/C, Pd cuboctahedron/C, Pd octahedron/C, and Pd concave/C). The suspension was washed six times with ultrapure water and ethanol through centrifugation. All Pd shape-controlled nanoparticles were uniformly distributed on carbon support (Figure S1).

Catalyst Characterizations. The concentrations of Pd element in suspensions were determined using an inductively coupled plasma mass spectrometer (ICP-MS, PerkinElmer Elan DRC). Each concentration in the suspension is 97.5 ppb of concave nanocubes, 93.3 ppb of octahedrons, and 86.2 ppb of cuboctahedrons. ICP-MS verified that all Pd shape-controlled nanoparticles are 20 wt % metal loading on the carbon support. Transmission electron microscopy (TEM) images were acquired to analyze the morphology and crystal structure using a HT7700 microscope operated at 120 kV (Hitachi). All shape-controlled nanoparticles were well dispersed in isopropyl alcohol suspensions, and the sample was prepared by drop casting on carbon-coated copper grids (FCF200-Cu, Electron Microscopy Science) and dried under ambient conditions in air.

Electrochemical Characterization. Electrochemical testing was conducted using a ring disk electrode (RDE) experimental setup (Pine Research) with a standard three-electrode electrochemical cell. A Pt wire counter electrode and Ag/AgCl (saturated potassium chloride) reference electrode were used. All potentials were converted to a reversible hydrogen electrode (RHE). Catalyst inks were prepared by mixing/dispersing the catalyst (1.5 mg mL^{–1}) and a Nafion ionomer solution (5 wt %, Sigma-Aldrich) (20 μL mL^{–1}) in the mixture of isopropyl alcohol and ultrapure water. After

ultrasonication for 20 min, 10 μL of uniformly dispersed ink was deposited onto a glassy carbon electrode (GCE). The Pd loading densities of all catalysts on GCEs were $25 \mu\text{g}_{\text{Pd}} \text{cm}^{-2}$, and the thin films on the surfaces of GCEs were dried under ambient conditions in air. Cyclic voltammetry was performed while rotating the shaft of the working electrode at 1000 rpm with a scan rate of 50 mV s^{-1} . The potential sweeps started at $0.2 V_{\text{RHE}}$ and repeated in a potential range of -0.2 to $0.8 V_{\text{RHE}}$. In all testing, an Ar-saturated 0.1 M NaOH aqueous solution containing 20 mM NaNO_3 or 2 mM NaNO_2 was used as the electrolyte. Alkaline conditions were deemed necessary to reduce the proton concentration to investigate intrinsic $\text{NO}_3\text{RR}/\text{NO}_2\text{RR}$ activity of Pd facets. In addition, the study of nitrate reduction in alkaline electrolytes provides insights into opportunities for treating alkaline waste streams. There are a number of industrial waste streams that exhibit high pH and nitrate concentrations, with nuclear-based waste streams being one such example.¹

Electrolysis testing was conducted with an H-type electrolytic cell separated by a Nafion 212 membrane, which is connected to an electrochemical workstation. The Nafion membrane was boiled in $3\% \text{ H}_2\text{O}_2$ for 1 h, ultrapure water for 2 h, and then $0.5 \text{ M H}_2\text{SO}_4$ for 1 h, sequentially. After the pretreatment, the membrane was thoroughly rinsed with ultrapure water several times. The working electrode was used as Pd-based catalysts that were spray-coated on carbon papers as a working electrode and Ag/AgCl was used as a reference electrode in the cathode chamber. Pt wire was used as a counter electrode and placed in the anode chamber. The geometric surface area of the working electrode was controlled with 0.4 cm^2 . The electrolyte in the H-type cell is the same as our previous half-cell test solution. The 0.1 M NaOH electrolyte was evenly distributed to the cathode and anode compartment, and 400 ppm of $\text{NO}_3^- \text{-N}$ was added into the only cathode compartment for NO_3RR with an Ar-purged environment. Chronoamperometry (CA) was performed at a potential of $-0.2 V_{\text{RHE}}$ for 1, 2, 3, and 4 h, respectively, for NO_3RR , detecting concentration variations of $\text{NO}_3^- \text{-N}$, $\text{NO}_2^- \text{-N}$, and $\text{NH}_3 \text{-N}$.

Product Measurements Analysis. The ultraviolet–visible (UV–vis) spectrophotometer was used to measure ion concentrations in electrolytes, collecting a small amount of samples after testing 1, 2, 3, and 4 h. $\text{NO}_3^- \text{-N}$ concentrations were estimated from absorption intensities at a wavelength of 345 nm that measured using the nitrate kit. $\text{NO}_2^- \text{-N}$ concentrations were determined from the absorption intensities at a wavelength of 540 nm that measured using a color reagent that is a mixture of *p*-aminobenzenesulfonamide (4 g), *N*-(1-Naphthyl) ethylenediamine dihydrochloride (0.2 g), ultrapure water (50 mL), and phosphoric acid (10 mL).⁴⁷ $\text{NH}_3 \text{-N}$ was measured using the indophenol blue method⁴⁸ conducted through extracting 1 mL of testing solutions after selected hours. In detail, 1 M NaOH solution containing 5 wt % salicylic acid and 5 wt % sodium citrate was initially added into samples, followed by the addition of 1 mL of 0.05 M NaClO and 0.1 mL of an aqueous solution of 1 wt % $\text{C}_5\text{FeN}_6\text{Na}_2\text{O}$ into 1 mL of samples. The formation of indophenol blue was detected in the absorbance at a wavelength of 655 nm . All calibration curves of $\text{NO}_3^- \text{-N}$, $\text{NO}_2^- \text{-N}$, and $\text{NH}_3 \text{-N}$ showed good linearity in an absorbance–concentration graph, and all samples were measured with a proper dilution to match each calibrate curve (Figure S2).

For the analysis of gaseous products, an in situ mass spectrometer (Cirrus 2, MKS Instruments) was connected to the H-cell. Ultrahigh purity Ar gas was fed into the cathode chamber in H-cell as a carrier gas at a flow rate of 20 mL min^{-1} during the measurement. All tests were initiated after the signal on the gas analyzer was stabilized.

Calculation of the NH_3 Yield, Conversion Rate, and Faradic Efficiency.

$$\text{NH}_3 \text{ yield} = \frac{C_{\text{NH}_3} \times V}{M_{\text{NH}_3} \times t \times A}$$

C_{NH_3} is the ion concentration of $\text{NH}_3(\text{aq})$, V is the electrolyte volume in the cathode compartment (20 mL including 400 ppm of $\text{NO}_3^- \text{-N}$), M_{NH_3} is the molar mass of NH_3 , t is the reduction time, and A is the working electrode area (0.4 cm^2)

$$\text{NO}_3^- \text{ conversion rate} = \frac{\Delta C_{\text{NO}_3^-}}{C_0} \times 100\%$$

$\Delta C_{\text{NO}_3^-}$ is the ion concentration difference of NO_3^- before and after reduction tests and C_0 is the initial ion concentration of NO_3^- .

$$\text{Faradaic efficiency (FE)} = \frac{n \times F \times C_{\text{NH}_3} \times V}{M_{\text{NH}_3} \times Q}$$

where n is the electrons involved in the formation of NH_3 (assumed $8 e^-$ reaction), F is the Faraday constant (96485 C mol^{-1}), C_{NH_3} is the ion concentration of $\text{NH}_3(\text{aq})$, V is the electrolyte volume (20 mL including 400 ppm of $\text{NO}_3^- \text{-N}$) in the cathode compartment, M_{NH_3} is the molar mass of NH_3 , and Q is the electric charge contributed to the formation of NH_3 .

Density Functional Theory (DFT) Calculations. The energy of chemical species adsorbed on Pd surfaces and in the aqueous phase was computed using density functional theory (DFT) implemented in the Vienna ab initio Package (VASP) version 5.4.4.⁴⁹ The core electrons were treated with the projector augmented-wave (PAW) method⁵⁰ employing default potentials in VASP.⁵¹ The valence electrons in each element treated explicitly were as follows: Pd— $4d^9 5s^1$, N— $2s^2 2p^3$, O— $2s^2 2p^4$, and H— $1s^1$. Exchange–correlation was described by the generalized gradient approximation (GGA) with the Perdew–Burke–Ernzerhof (PBE) functional.⁵² All calculations employed spin polarization. The Methfessel–Paxton smearing method⁵³ was applied with 0.2 eV smearing width. The plane-wave basis set was truncated with a 400 eV kinetic energy cutoff. The Brillouin zone was sampled by a Monkhorst–Pack (MP)⁵⁴ k -point grid with $5 \times 5 \times 1$ and $6 \times 6 \times 1$ spacing for Pd(111) and Pd(100), respectively. A dipole correction in the z -direction was applied for all structure optimizations in vacuum, and a solvation single-point correction was applied to all optimized geometries using the VASPsol^{55,56} method with default parameter settings and a dielectric constant of 78.4 for water. van der Waals interactions were described by Grimme D3 dispersion.⁵⁷

Four layers of Pd(111) and Pd(100) surfaces were generated from a bulk Pd structure with an optimized lattice parameter of 3.89 \AA , which agrees with the literature value.⁵⁸ The bottom layer of the slab was fixed in all calculations. The distance separating the periodic Pd slabs in the z -direction was at least 15 \AA in all cases. Atomic coordinates were optimized until the maximum force between the atoms was less than 0.02 eV/\AA .

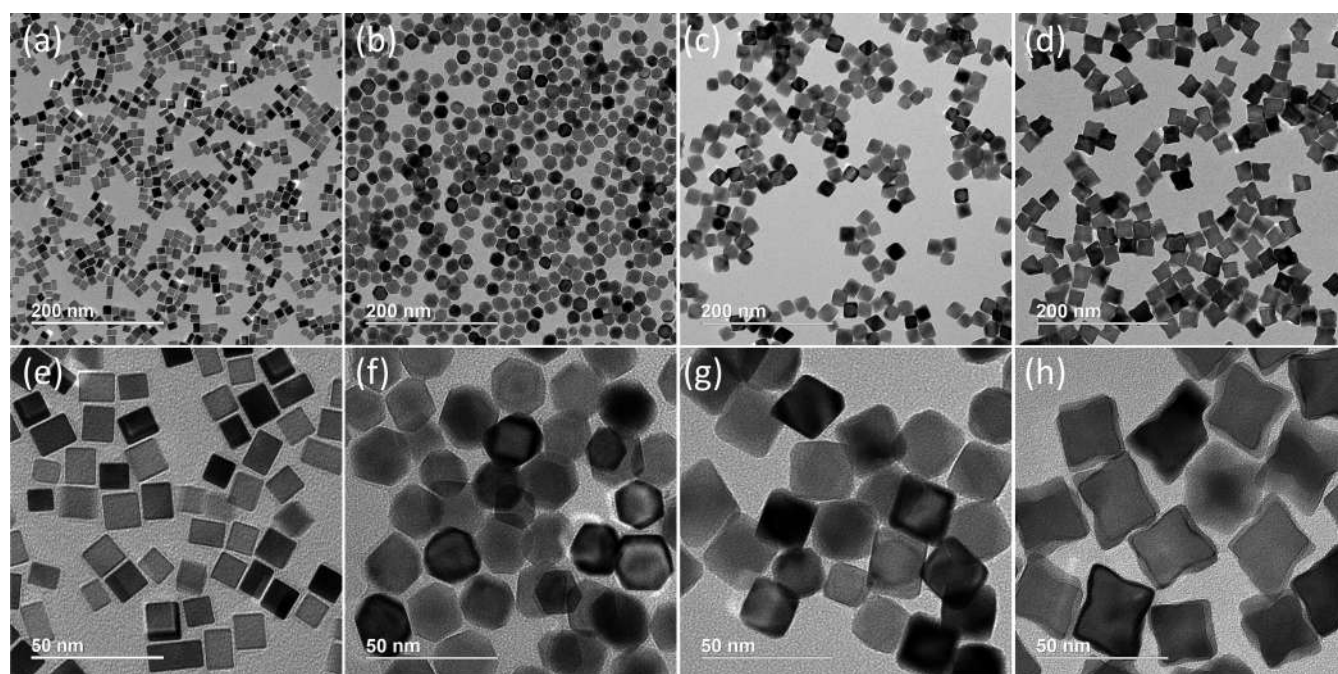


Figure 1. TEM images of Pd shape-controlled nanoparticles. (a, e) Pd nanocube, (b, f) Pd cubooctahedron, (c, g) Pd octahedron, and (d, h) Pd concave nanocube. Enlarged images in low-magnification TEM are shown in Figure S3.

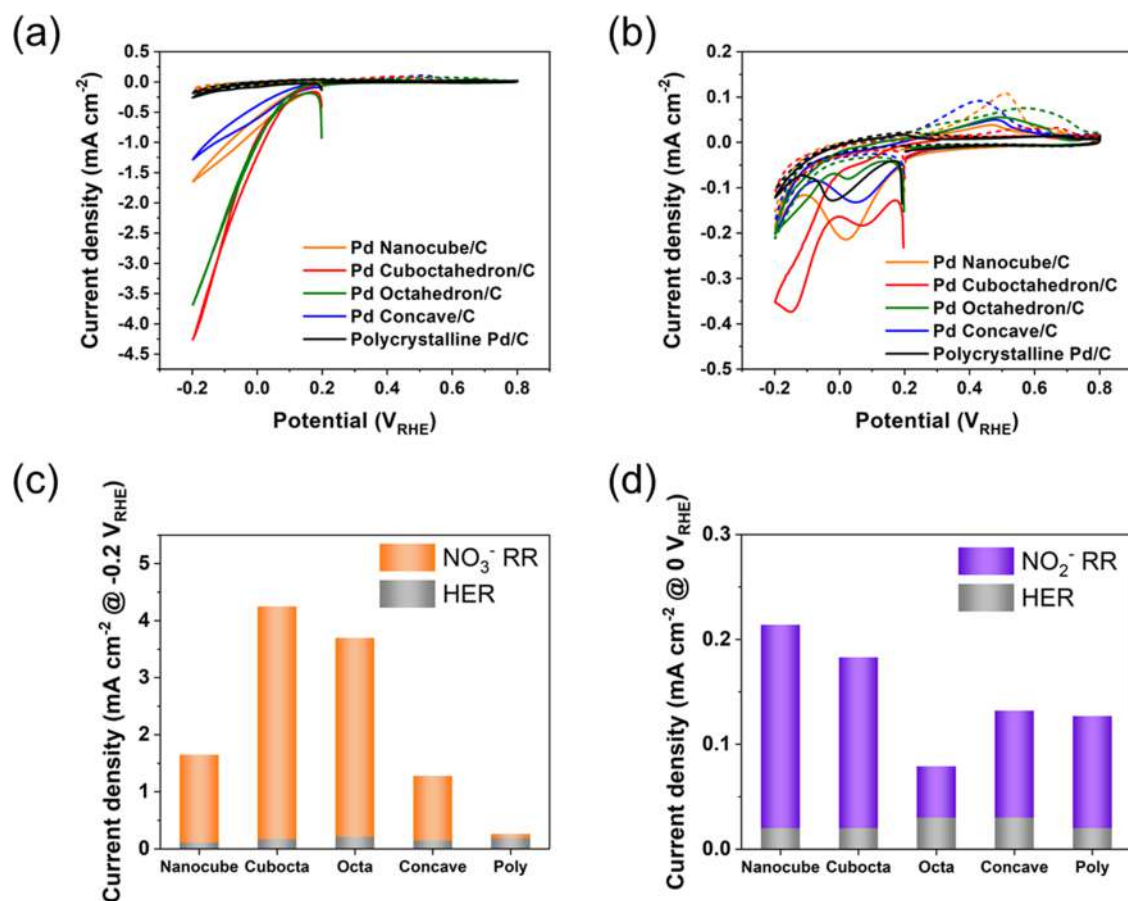


Figure 2. Electrochemical activity of (a) NO₃RR and (b) NO₂RR for all Pd catalysts over HER. Dash lines are blank CV tests for all Pd catalysts at Ar-saturated 0.1 M NaOH in the absence of 20 mM NO₃⁻ or 2 mM NO₂⁻, whereas solid lines are CV tests at Ar-saturated 0.1 M NaOH in the presence of 20 mM NO₃⁻ or 2 mM NO₂⁻. (c, d) Current density was collected at -0.2 V_{RHE} for (c) NO₃RR and peaks around 0 V_{RHE} for (d) NO₂RR for all Pd catalysts.

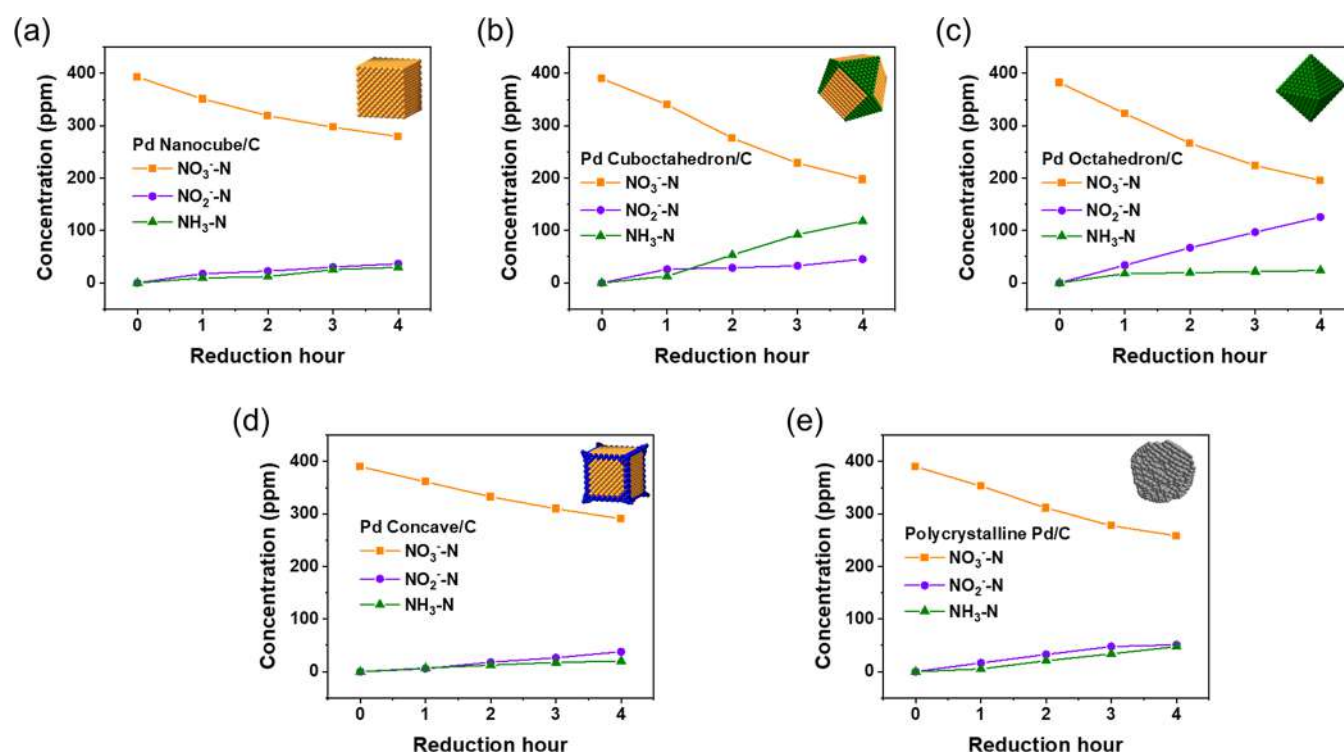
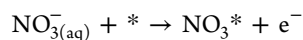


Figure 3. Concentration change of NO_3^- -N, NO_2^- -N, and NH_3 -N over reaction time during chronoamperometry tests using an H-cell at $-0.2 V_{\text{RHE}}$ for (a) Pd nanocube/C, (b) Pd cubooctahedron/C, (c) Pd octahedron/C, (d) Pd concave/C, and (e) polycrystalline Pd/C.

The energies of HNO_3 , HNO_2 , and H_2 were computed in a $15 \times 15 \times 15 \text{ \AA}^3$ unit cell with $1 \times 1 \times 1$ MP k -points sampling. Transition states were found using the climbing image nudged elastic band (CI-NEB) method.^{59,60} Translational, rotational, and vibrational corrections to the free energy were incorporated using standard formulas from statistical mechanics for gaseous species. Only vibrational corrections were considered for adsorbed species on Pd surfaces.

We used the computational hydrogen electrode (CHE)⁶¹ to estimate the adsorption energy of nitrate and the desorption energy of nitrite as a function of the applied potential. The reaction equation for nitrate adsorption is

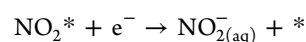


The free energy for this reaction, $\Delta G_{\text{ads}}(\text{NO}_3^-)$, is computed using the following expression, where a thermodynamic cycle is employed to avoid direct calculations involving the solvated nitrate anion in the periodic simulation cell

$$\begin{aligned} \Delta G_{\text{ads}}(\text{NO}_3^-) &= G_{\text{NO}_3^*} + [G_{e^-} + G_{\text{H}^+}] - [G_{\text{NO}_3^-} + G_{\text{H}^+}] \\ &\quad - G_* \\ &= G_{\text{NO}_3^*} - G_* + \left[\frac{1}{2} G_{\text{H}_2} - eU_{\text{RHE}} \right] \\ &\quad - [G_{\text{HNO}_3} + 2.303 \text{ RT} (\text{p}K_a - \text{pH})] \end{aligned}$$

where $G_{\text{NO}_3^*}$ is the free energy of $^*\text{NO}_3$ adsorbed on the Pd surface, G_{e^-} is the free energy of the electron, G_{H^+} is the free energy of the proton, $G_{\text{NO}_3^-}$ is the free energy of nitrate in solution, G_* is the energy of the Pd surface, e is the elementary positive charge, U_{RHE} is the applied potential referenced to the reversible hydrogen electrode (RHE), G_{H_2} is the free energy of gaseous H_2 at 1 bar, G_{HNO_3} is the free energy of aqueous

HNO_3 , R is the gas constant, T is the temperature, and $\text{p}K_a$ is computed from the experimental⁶² acid dissociation constant of HNO_3 (i.e., $\text{p}K_a = -1.4$). The thermodynamic cycle ensures that the free energy of the proton contained in the CHE expression and in the acid dissociation expression cancels at $\text{pH} = 0$. Adsorption/desorption energies can be corrected for any arbitrary pH by simply correcting the free energy of the proton by 2.303 RT pH . Here, this correction would be identical for both surface facets, so the relative difference in adsorption/desorption energies between the two facets does not depend on pH. Similarly, the reaction equation for nitrite desorption is



The free energy of the reaction, $\Delta G_{\text{des}}(\text{NO}_2^-)$, is also computed with a thermodynamic cycle

$$\begin{aligned} \Delta G_{\text{des}}(\text{NO}_2^-) &= G_* - G_{\text{NO}_2^*} - \left[\frac{1}{2} G_{\text{H}_2} - eU_{\text{RHE}} \right] \\ &\quad + [G_{\text{HNO}_2} + 2.303 \text{ RT} (\text{p}K_a - \text{pH})] \end{aligned}$$

where $G_{\text{NO}_2^*}$ is the free energy of NO_2 adsorbed on the Pd surface, G_{HNO_2} is the free energy of aqueous HNO_2 , and $\text{p}K_a$ is computed from the experimental⁶³ acid dissociation constant of HNO_2 (i.e., $\text{p}K_a = 3.25$). The reaction energies, reported in Table S1, were computed at 298.15 K; the pressure and concentration for $\text{H}_2(\text{g})$, $\text{HNO}_3(\text{aq})$, and $\text{HNO}_2(\text{aq})$ are 1 atm, 400 ppm, and 10 ppm, respectively.

RESULTS AND DISCUSSION

All Pd shape-controlled nanoparticles exhibited well-defined shapes and structures (Figures 1 and S3). The Pd nanocube was enclosed by six $\{100\}$ facets with an average edge length of

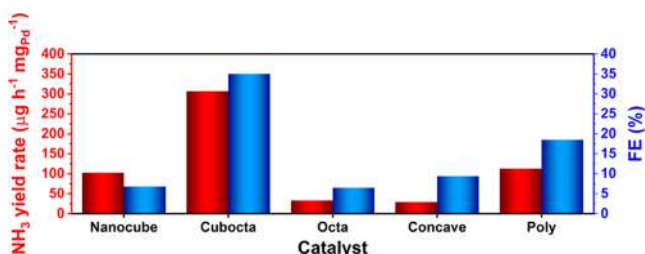


Figure 4. NH₃ yield rate at 3 h and faradaic efficiency (FE) of all Pd catalysts.

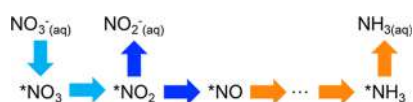


Figure 5. Reaction mechanism for nitrate reduction toward nitrite and ammonia.

13.0 nm. The Pd cuboctahedron contained six {100} and eight {111} facets with an average edge length of 20.5 nm. The Pd octahedron had eight {111} facets with an average edge length of 21.9 nm. Finally, the Pd concave nanocube had {100} facets at the terrace and high-index {*hk0*} facets such as (730)⁶⁴ at the edges/vertex with an average edge length of 19.0 nm. These well-defined surface structures contrast with that of polycrystalline Pd nanoparticles (commercial Pd/C, 3–5 nm), which are typically enclosed by randomly mixed facets of {111}, {200}, {220}, and {311} facets.^{65,66}

Activity of Electrochemical NO₃RR and NO₂RR on Pd Nanocrystals. The electrochemical activities for NO₃RR (rate-determining step) and NO₂RR (selectivity determining step) were determined through cyclic voltammetry (CV) (Figure 2a,2b). Current density is normalized by the

electrochemical surface area (ECSA) of each Pd catalyst (Figure S4 and Table S2). Blank CVs in the absence of reactant (either nitrate or nitrite) were measured in an Ar-saturated 0.1 M NaOH electrolyte (dash lines in Figure 2a,b). All of the Pd catalysts showed almost identical blank CV curves with low current densities ($\sim 0.2 \text{ mA cm}^{-2}$ at $-0.2 \text{ V}_{\text{RHE}}$). These results are expected as the only reaction which can proceed is the HER reaction, and alkaline conditions limit the HER reaction. Electrochemical NO₃RR activity of all Pd catalysts was evaluated in the presence of nitrate ions (20 mM NO₃⁻) at an Ar-saturated 0.1 M NaOH electrolyte (solid lines in Figure 2a). Due to the low HER activity, current from the CVs arises primarily due to the NO₃⁻ reduction reaction (Figure 2c). NO₃⁻ reduction at potentials between $-0.2 \text{ V}_{\text{RHE}}$ and 0 V_{RHE} demonstrated an increased current with respect to the blank CV. At $-0.2 \text{ V}_{\text{RHE}}$, the current density was 4.25 mA cm^{-2} for Pd cuboctahedron/C, 3.70 mA cm^{-2} for Pd octahedron/C, 1.65 mA cm^{-2} for the Pd nanocube/C, 1.28 mA cm^{-2} for the Pd concave/C, and 0.26 mA cm^{-2} for the commercial Pd/C (denote polycrystalline Pd/C). Thus, the activity for NO₃RR was Pd cuboctahedron/C > Pd octahedron/C > Pd nanocube/C > Pd concave/C > polycrystalline Pd/C. It is noteworthy that the primary feature of cuboctahedron and octahedron is the presence of eight {111} facets, which do not exist in the nanocube nor concave cube. Thus, the electrochemical activity toward NO₃RR on Pd decreases in the order (111) > (100) > (*hk0*). Polycrystalline Pd nanoparticles may be enclosed mainly by the (220) and (311) facets as they show even lower NO₃RR activity relative to the other shape-controlled Pd nanoparticles. The highest ECSA and less well-defined structure of polycrystalline Pd also exhibited the lowest current density and NO₃RR activity.

The electrochemical activity for NO₂RR was next determined through CV with and without nitrite ions (Figure

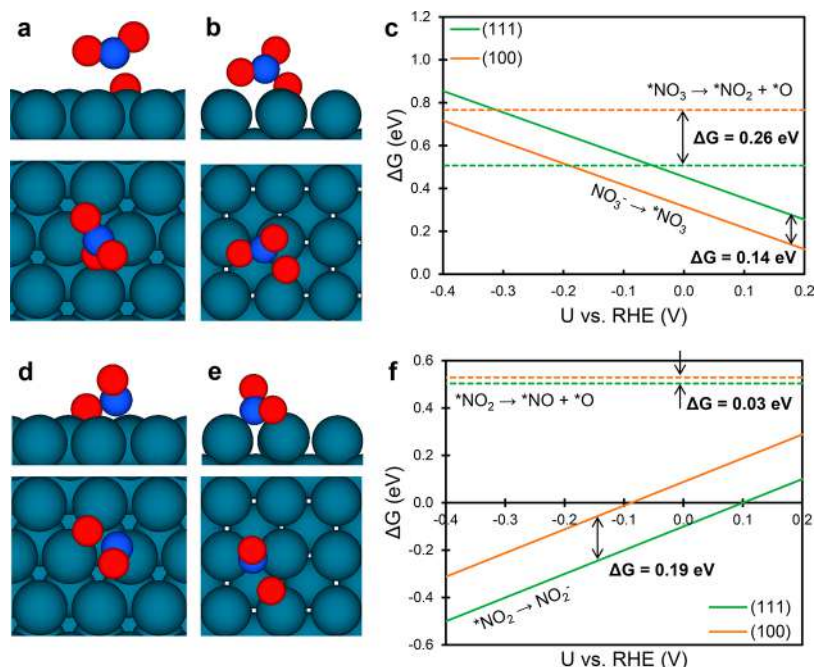


Figure 6. (a, b) Top and side views of the transition state of $*\text{NO}_3 \rightarrow *\text{NO}_2$ on (a) Pd(111) and (b) Pd(100). (c) Energy of NO₃⁻ adsorption at pH = 0 and the activation barrier for $*\text{NO}_3 \rightarrow *\text{NO}_2$ plotted against the applied potential. (d, e) Top and side views of the transition state of $*\text{NO}_2 \rightarrow *\text{NO}$ on (d) Pd(111) and (e) Pd(100). (f) Energy of NO₂⁻ desorption at pH = 0 and the activation barrier for $*\text{NO}_2 \rightarrow *\text{NO}$ plotted against the applied potential. The red, blue, and green spheres represent O, N, and Pd, respectively.

2b). The electrochemical NO₂RR activities of all of the shape-controlled Pd/C in the presence of nitrite ions (2 mM NO₂⁻) were measured in Ar-saturated 0.1 M NaOH electrolyte. NO₂⁻ reduction occurred around 0 V_{RHE}.³⁸ At the peak, the current density was 0.214 mA cm⁻² for Pd nanocube/C, 0.183 mA cm⁻² for Pd cuboctahedron/C, 0.132 mA cm⁻² for Pd concave/C, 0.127 mA cm⁻² for polycrystalline Pd/C, and 0.079 mA cm⁻² for Pd octahedron/C. Thus, the activity for NO₂RR was Pd nanocube/C > Pd cuboctahedron/C > Pd concave/C > polycrystalline Pd/C > Pd octahedron/C. Note that the primary feature of the Pd nanocube is enclosed by only the (100) facet, suggesting that the (100) facet may have higher NO₂RR activity than Pd(111) or Pd(*hk0*). Here, the polycrystalline Pd catalyst showed higher activity than Pd octahedron/C for NO₂RR. This result indicates that (100) facet is critical, which further highlights the origin of polycrystalline Pd high NO₂RR activity. Again, the activity changes observed were not due to changes in HER activity, which remained consistent and low in all tests (Figure 2d).

Selectivity of Electrochemical NO₃RR and NO₂RR on Pd Nanocrystals. The NO₃⁻-N removal efficiency over 4 h at -0.2 V_{RHE} applied potential was 49.4% for Pd cuboctahedron/C, 48.8% for Pd octahedron/C, 33.8% of polycrystalline Pd/C, 28.9% of Pd nanocube/C, and 25.6% of Pd concave/C (Figure 3a–e). This is in line with the activity measurements, where the highest current for the activity-determining step occurred on Pd cuboctahedron/C and Pd octahedron/C. Thus, again the presence of Pd (111) facets results in high conversion of nitrate.

The critical products that form because of NO₃RR are NO₂⁻-N, NH₃⁻-N, N₂-N, and potentially H₂. In all batch electrolysis tests, in situ mass spectrometer measurements confirmed that H₂ was the only detected gaseous product for NO₃RR of Pd catalysts at CA -0.2 V_{RHE} in 0.1 M NaOH solution. N₂, N₂O, and NO gaseous products were not detected (Figure S5). The lack of selectivity toward nitrogen is due to the Pd surface not producing N₂O, which is being inhibited by low NO* coverage that is essential for lowering the N₂O* formation barrier on Pd. The N₂O formation is a necessary intermediate needed to produce N₂ in alkaline electrolytes.^{10,67} Furthermore, the high affinity of Pd for adsorbed hydrogen aids in reducing NO₃⁻ to NH₃.^{68–71} Note that the total nitrogen balance after 4 h electrolysis was not exactly the same as the initial nitrate concentrations (Table S3). This is because many intermediates form in the transformation process. We anticipate that other predominate N intermediates not measured are NO, N₂H₄, and NH₂OH. Since NO was not detected in mass spectrometry measurements, it may be adsorbed to the catalyst surface in low concentrations.

NH₃-N production over 4 h at -0.2 V_{RHE} applied potential was 118 ppm for the Pd cuboctahedron/C, 47.8 ppm for the polycrystalline Pd/C, 29.8 ppm of Pd nanocube/C, 23.8 ppm for Pd octahedron/C, and 20.4 ppm of Pd concave/C (Figure 3a–e). This indicates that the presence of Pd(111) is critical for enabling conversion of NO₃⁻ to NO₂⁻, and that Pd(100) facets were beneficial for removing NO₂⁻-N and effectively converted from NO₂⁻-N to NH₃-N. Thus, although Pd octahedron/C exhibited high activity (Figure 2a,2c), electrochemically formed NO₂⁻-N remained stable under further conversion. This result shows that the reaction on the Pd(111) facet is unfavorable because this facet reduces NO₂⁻-N compared to other Pd facets, resulting in less produced

NH₃-N. Cuboctahedron is a uniform polyhedron enclosed by eight (111) facets and six (100) facets, which contains 24 edges as a boundary. Thanks to many edges in Pd cuboctahedron, after NO₃⁻-N reduction passing through (111) facets, desorbed NO₂⁻-N from (111) facets can be directly readsorbed and reacted on (100) facets with high accessibility of neighbor (100) facets, resulting in producing the highest amount of NH₃.

Pd cuboctahedron/C exhibited the highest NH₃ yield rate and FE (307 μg h⁻¹ mg_{Pd}⁻¹, 35.1%) compared to polycrystalline Pd/C (113 μg h⁻¹ mg_{Pd}⁻¹, 18.5%), Pd nanocube/C (103 μg h⁻¹ mg_{Pd}⁻¹, 6.76%), Pd octahedron/C (32.9 μg h⁻¹ mg_{Pd}⁻¹, 6.50%), and Pd concave/C (29.2 μg h⁻¹ mg_{Pd}⁻¹, 9.36%) (Figure 4). The FE of the process from nitrate to ammonia was relatively low because of the faster competitive HER and the complicated pathways from nitrate to ammonia, which produces a number of N species intermediates such as NO_x, N₂H₄, and NH₂OH. The major FE excluding ammonia formation is derived from HER because Pd nanocrystals could not produce any other gaseous products except hydrogen. Pd nanocube enclosed by {100} facets showed higher HER activity than Pd octahedron enclosed by {111} facets, experimentally and theoretically.⁷² Higher HER activity of Pd nanocube could contribute to achieving lower FE for ammonia. The lower HER activity of Pd octahedron enclosed by {111} facets showed higher nitrate reduction activity because of more suppressing HER than Pd nanocube. However, Pd {111} showed the lowest nitrite reduction activity. Thus, not only suppressing HER, but the formation of tandem coordination of nitrate-to-nitrite and nitrite-to-NO reactions is important. Nanocrystals also exhibited excellent structure stability after electrochemical NO₃RR tests (Figure S6). The shapes of Pd catalysts were maintained with their well-extended facets without severe agglomeration of nanoparticles. Pd shape-controlled nanoparticles showed highly active and different performance by facets, and highly stable after testing at CA -0.2 V_{RHE} in 0.1 M NaOH electrolyte.

The effect of size of Pd NPs for NH₃ yield was examined by annealing at 700 °C (Pd/C-700C, 27.8 nm) and 800 °C (Pd/C-800C, 48.2 nm) for 1 h in the Ar/H₂ gas environment using polycrystalline Pd/C (commercial Pd/C, 3–5 nm) (Figure S8). Polycrystalline Pd/C, Pd/C-700C, and Pd/C-800C showed very similar NH₃ yields regardless of different Pd NP sizes (Figure S9). This result demonstrated that ECSA has little impact on the selectivity for NH₃ yields.⁴⁷ Compared to Pd cuboctahedron/C and polycrystalline Pd/C, Pd cuboctahedron/C (307 μg mg_{Pd}⁻¹ h⁻¹) showed higher NH₃ yield rate than polycrystalline Pd/C (113 μg mg_{Pd}⁻¹ h⁻¹), Pd/C-700C (114 μg mg_{Pd}⁻¹ h⁻¹), and Pd/C-800C (118 μg mg_{Pd}⁻¹ h⁻¹). This is because (220), (311), high-index facets (*hk0*), and lack of well-defined edge sites between (111) and (100) facets for desorption/adsorption were not facilitated to electrochemical kinetics from NO₃⁻ to NH₃.

Theoretical Investigation on the Nitrate Reduction Mechanism. Important aspects of the nitrate reduction mechanism on transition-metal catalysts established in the literature^{9,24,73} are summarized in Figure 5. Catalytic activity is determined by the first step of nitrate adsorption and conversion to nitrite (light-blue arrows in the figure), while selectivity toward nitrite versus ammonia is controlled by the favorability of *NO₂ desorption versus dissociation to *NO (dark-blue arrows in the figure). Thus, we use DFT to study

the difference in the energetic favorability of these steps between Pd(111) and Pd(100).

We first compared the favorability of nitrate adsorption and dissociation on the two surfaces (Figure 6a–c). Figure 6c shows that nitrate adsorbs more favorably on Pd(100) compared to Pd(111) by 0.14 eV. However, the barrier for $^*\text{NO}_3$ dissociation is 0.26 eV lower on Pd(111) compared to Pd(100). Thus, the apparent barrier for nitrate adsorption and dissociation (i.e., the nitrate adsorption energy and $^*\text{NO}_3$ dissociation barrier summed) is 0.12 eV higher on Pd(100) than on Pd(111). This implies that Pd clusters that expose the Pd(111) facet will exhibit faster nitrate reduction, in agreement with the experimental observation that cuboctahedron and octahedron Pd have higher NO_3RR activity (Figure 2a,2c). Turning to the nitrite desorption step versus the dissociation step, we find that the activation barrier for $^*\text{NO}_2$ dissociation to $^*\text{NO}$ is similar on Pd(100) and Pd(111) (Figure 6d–f). However, $^*\text{NO}_2$ desorption is 0.19 eV more favorable on Pd(111) compared to Pd(100), implying that nitrite will desorb more readily from the Pd(111) surface before it can dissociate and form ammonia. Thus, the Pd nanocube exposing Pd(100) is more active than the octahedron exposing Pd(111) during NO_2RR , in agreement with Figure 2b,2d. $^*\text{NO}_2$ dissociation is less likely to occur on Pd(111), which results in the selective nitrite production exhibited by the Pd octahedron (Figure 3c). In contrast, $^*\text{NO}_2$ adsorbs on Pd(100) surfaces more strongly, and thus ammonia formation is favored on Pd nanocubes. The simulation results confirm that Pd(111) can more readily catalyze the initial nitrate reduction step to form nitrite, while Pd(100) can more readily catalyze nitrite reduction to form ammonia. This explains the high activity and selectivity toward ammonia achieved by Pd cuboctahedron structures that expose both the Pd(111) and Pd(100) facets that can work in tandem to catalyze the full reaction to form ammonia.

CONCLUSIONS

We synthesized Pd shape-controlled electrocatalysts with various well-exposed Pd facets and deposited each catalyst on a carbon support. All shape-controlled Pd catalysts showed high and different NO_3RR activity and excellent shape stability after performing NO_3RR and NO_2RR in an alkaline electrolyte. DFT simulations demonstrated that Pd(111) facets exhibit faster NO_3RR kinetics due to a lower $^*\text{NO}_3$ dissociation barrier, while Pd(100) facets exhibit higher selectivity to NH_3 over NO_2^- because $^*\text{NO}_2$ adsorbs more strongly on Pd(100) than on Pd(111). Pd cuboctahedron/C showed the highest NH_3 yield rate and FE because Pd cuboctahedron/C is enclosed by eight (111) facets and six (100) facets; the (111) facets rapidly activate and reduce NO_3^- to NO_2^- and the (100) facets reduce NO_2^- to NH_3 . Thus, controlling the structure and facets of Pd nanoparticles can enhance NH_3 production. This provides fundamental insights into the rational design of NO_3RR electrocatalysts for efficiently transforming nitrate into NH_3 .

ASSOCIATED CONTENT

Supporting Information

The Supporting Information is available free of charge at <https://pubs.acs.org/doi/10.1021/acscatal.1c01413>.

TEM images at low magnification of all shape-controlled Pd catalysts; TEM images for Pd deposition on carbon

support; ECSA calculation methods and summarizes; UV–vis measurements; The absorbance–concentration calibration curves of NO_3^- -N, NO_2^- -N, and NH_3 -N; in situ mass spectrometer results; TEM results for stability after testing; nitrate and nitrite reduction activity of Vulcan carbon XC72R; additional H-cell test with carbon paper electrode and OCV tests of all Pd catalysts for verifying contaminations; Total nitrogen balance before and after electrolysis; size effects on NH_3 yield of Pd with larger sizes by annealing; and additional computational details and results (PDF)

AUTHOR INFORMATION

Corresponding Authors

Thomas P. Senf – Department of Chemical and Biomolecular Engineering, Rice University, Houston, Texas 77005, United States; orcid.org/0000-0002-5889-5009; Email: tsenf@rice.edu

Seung Woo Lee – George W. Woodruff School of Mechanical Engineering, Georgia Institute of Technology, Atlanta, Georgia 30332, United States; orcid.org/0000-0002-2695-7105; Email: seung.lee@me.gatech.edu

Marta C. Hatzell – George W. Woodruff School of Mechanical Engineering, Georgia Institute of Technology, Atlanta, Georgia 30332, United States; orcid.org/0000-0002-5144-4969; Email: marta.hatzell@me.gatech.edu

Authors

Jeonghoon Lim – George W. Woodruff School of Mechanical Engineering, Georgia Institute of Technology, Atlanta, Georgia 30332, United States

Chun-Yen Liu – Department of Chemical and Biomolecular Engineering, Rice University, Houston, Texas 77005, United States

Jinho Park – George W. Woodruff School of Mechanical Engineering, Georgia Institute of Technology, Atlanta, Georgia 30332, United States; Aerospace, Transportation and Advanced Systems Laboratory, Georgia Tech Research Institute, Georgia Institute of Technology, Atlanta, Georgia 30332, United States

Yu-Hsuan Liu – School of Civil and Environmental Engineering, Georgia Institute of Technology, Atlanta, Georgia 30332, United States

Complete contact information is available at: <https://pubs.acs.org/doi/10.1021/acscatal.1c01413>

Notes

The authors declare no competing financial interest.

ACKNOWLEDGMENTS

This material is based upon the work supported by the National Science Foundation under Grant nos 1846611 and 1933646. CYL and TPS acknowledge support from an Interdisciplinary Excellence Award furnished by the Creative Ventures program at Rice University.

REFERENCES

- (1) van Langevelde, P. H.; Katsounaros, I.; Koper, M. T. Electrocatalytic Nitrate Reduction for Sustainable Ammonia Production. *Joule* **2021**, *5*, 290–294.
- (2) Duca, M.; Koper, M. T. Powering Denitrification: The Perspectives of Electrocatalytic Nitrate Reduction. *Energy Environ. Sci.* **2012**, *5*, 9726–9742.

- (3) Singh, N.; Goldsmith, B. R. Role of Electrocatalysis in the Remediation of Water Pollutants. *ACS Catal.* **2020**, *10*, 3365–3371.
- (4) Martínez, J.; Ortiz, A.; Ortiz, I. State-of-the-art and Perspectives of the Catalytic and Electrocatalytic Reduction of Aqueous Nitrates. *Appl. Catal., B* **2017**, *207*, 42–59.
- (5) Jensen, V. B.; Darby, J. L.; Seidel, C.; Gorman, C. Nitrate in Potable Water Supplies: Alternative Management Strategies. *Crit. Rev. Environ. Sci. Technol.* **2014**, *44*, 2203–2286.
- (6) Vorlop, K.-D.; Tacke, T. Erste Schritte auf dem Weg zur edelmetallkatalysierten Nitrat- und Nitrit-Entfernung aus Trinkwasser. *Chem. Ing. Tech.* **1989**, *61*, 836–837.
- (7) Jia, R.; Wang, Y.; Wang, C.; Ling, Y.; Yu, Y.; Zhang, B. Boosting Selective Nitrate Electroreduction to Ammonium by Constructing Oxygen Vacancies in TiO₂. *ACS Catal.* **2020**, *10*, 3533–3540.
- (8) Garcia-Segura, S.; Lanzarini-Lopes, M.; Hristovski, K.; Westerhoff, P. Electrocatalytic Reduction of Nitrate: Fundamentals to Full-scale Water Treatment Applications. *Appl. Catal., B* **2018**, *236*, 546–568.
- (9) Liu, J.-X.; Richards, D.; Singh, N.; Goldsmith, B. R. Activity and Selectivity Trends in Electrocatalytic Nitrate Reduction on Transition Metals. *ACS Catal.* **2019**, *9*, 7052–7064.
- (10) de Vooy, A. C. A.; Van Santen, R.; Van Veen, J. Electrocatalytic Reduction of NO₃⁻ on Palladium/copper Electrodes. *J. Mol. Catal. A: Chem.* **2000**, *154*, 203–215.
- (11) Álvarez, B.; Rodes, A.; Perez, J.; Feliu, J.; Rodriguez, J.; Pastor, E. Spectroscopic Study of the Nitric Oxide Adlayers Formed from Nitrous Acid Solutions on Palladium-covered Platinum Single-crystal Electrodes. *Langmuir* **2000**, *16*, 4695–4705.
- (12) Horányi, G.; Rizmayer, E. Role of Adsorption Phenomena in the Electrocatalytic Reduction of Nitric Acid at a Platinized Platinum Electrode. *J. Electroanal. Chem. Interfacial Electrochem.* **1982**, *140*, 347–366.
- (13) Dima, G. E.; De Vooy, A.; Koper, M. Electrocatalytic Reduction of Nitrate at Low Concentration on Coinage and Transition-metal Electrodes in Acid Solutions. *J. Electroanal. Chem.* **2003**, *554–555*, 15–23.
- (14) Li, H.; Guo, S.; Shin, K.; Wong, M. S.; Henkelman, G. Design of a Pd–Au Nitrite Reduction Catalyst by Identifying and Optimizing Active Ensembles. *ACS Catal.* **2019**, *9*, 7957–7966.
- (15) Shuai, D.; McCalman, D. C.; Choe, J. K.; Shapley, J. R.; Schneider, W. F.; Werth, C. J. Structure Sensitivity Study of Waterborne Contaminant Hydrogenation Using Shape- and Size-controlled Pd Nanoparticles. *ACS Catal.* **2013**, *3*, 453–463.
- (16) Shin, H.; Jung, S.; Bae, S.; Lee, W.; Kim, H. Nitrite Reduction Mechanism on a Pd surface. *Environ. Sci. Technol.* **2014**, *48*, 12768–12774.
- (17) Prüsse, U.; Hähnlein, M.; Daum, J.; Vorlop, K.-D. Improving the Catalytic Nitrate Reduction. *Catal. Today* **2000**, *55*, 79–90.
- (18) Gootzen, J. F. E.; Peeters, P.; Dukers, J.; Lefferts, L.; Visscher, W.; Van Veen, J. The Electrocatalytic Reduction of NO₃⁻ on Pt, Pd and Pt+ Pd Electrodes Activated with Ge. *J. Electroanal. Chem.* **1997**, *434*, 171–183.
- (19) Rosca, V.; Duca, M.; de Groot, M. T.; Koper, M. T. Nitrogen Cycle Electrocatalysis. *Chem. Rev.* **2009**, *109*, 2209–2244.
- (20) Birdja, Y. Y.; Yang, J.; Koper, M. Electrocatalytic Reduction of Nitrate on Tin-modified Palladium Electrodes. *Electrochim. Acta* **2014**, *140*, 518–524.
- (21) Sá, J.; Gasparovicova, D.; Hayek, K.; Halwax, E.; Anderson, J. A.; Vinek, H. Water Denitration over a Pd–Sn/Al₂O₃ Catalyst. *Catal. Lett.* **2005**, *105*, 209–217.
- (22) Petrii, O. A.; Safonova, T. Y. Electroreduction of Nitrate and Nitrite Anions on Platinum Metals: A Model Process for Elucidating the Nature of the Passivation by Hydrogen Adsorption. *J. Electroanal. Chem.* **1992**, *331*, 897–912.
- (23) Kamiya, K.; Tatebe, T.; Yamamura, S.; Iwase, K.; Harada, T.; Nakanishi, S. Selective Reduction of Nitrate by a Local Cell Catalyst Composed of Metal-Doped Covalent Triazine Frameworks. *ACS Catal.* **2018**, *8*, 2693–2698.
- (24) Guo, S.; Heck, K.; Kasiraju, S.; Qian, H.; Zhao, Z.; Grabow, L. C.; Miller, J. T.; Wong, M. S. Insights into Nitrate Reduction over Indium-Decorated Palladium Nanoparticle Catalysts. *ACS Catal.* **2018**, *8*, 503–515.
- (25) de Vooy, A. C. A.; Koper, M.; Van Santen, R.; Van Veen, J. Mechanistic Study on the Electrocatalytic Reduction of Nitric Oxide on Transition-Metal Electrodes. *J. Catal.* **2001**, *202*, 387–394.
- (26) Ebbesen, S. D.; Mojet, B. L.; Lefferts, L. In situ ATR-IR Study of Nitrite Hydrogenation over Pd/Al₂O₃. *J. Catal.* **2008**, *256*, 15–23.
- (27) Zhang, R.; Shuai, D.; Guy, K. A.; Shapley, J. R.; Strathmann, T. J.; Werth, C. J. Elucidation of Nitrate Reduction Mechanisms on a Pd–In Bimetallic Catalyst using Isotope Labeled Nitrogen Species. *ChemCatChem* **2013**, *5*, 313–321.
- (28) Katsounaros, I.; Figueiredo, M. C.; Chen, X.; Calle-Vallejo, F.; Koper, M. T. Interconversions of Nitrogen-containing Species on Pt (100) and Pt (111) Electrodes in Acidic Solutions Containing Nitrate. *Electrochim. Acta* **2018**, *271*, 77–83.
- (29) Katsounaros, I.; Chen, T.; Gewirth, A. A.; Markovic, N. M.; Koper, M. T. Evidence for Decoupled Electron and Proton Transfer in the Electrochemical Oxidation of Ammonia on Pt (100). *J. Phys. Chem. Lett.* **2016**, *7*, 387–392.
- (30) Duca, M.; Sacré, N.; Wang, A.; Garbarino, S.; Guay, D. Enhanced Electrocatalytic Nitrate Reduction by Preferentially-oriented (100) PtRh and PtIr alloys: The Hidden Treasures of the ‘Miscibility Gap’. *Appl. Catal., B* **2018**, *221*, 86–96.
- (31) Taguchi, S.; Feliu, J. M. Electrochemical Reduction of Nitrate on Pt (S)[n (1 1 1) × (1 1 1)] Electrodes in Perchloric Acid Solution. *Electrochim. Acta* **2007**, *52*, 6023–6033.
- (32) Taguchi, S.; Feliu, J. M. Kinetic Study of Nitrate Reduction on Pt (1 1 0) Electrode in Perchloric Acid Solution. *Electrochim. Acta* **2008**, *53*, 3626–3634.
- (33) Kerkeni, S.; Lamy-Pitara, E.; Barbier, J. Copper–Platinum Catalysts Prepared and Characterized by Electrochemical Methods for the Reduction of Nitrate and Nitrite. *Catal. Today* **2002**, *75*, 35–42.
- (34) Figueiredo, M. C.; Souza-Garcia, J.; Climent, V.; Feliu, J. M. Nitrate Reduction on Pt (1 1 1) Surfaces Modified by Bi Adatoms. *Electrochem. Commun.* **2009**, *11*, 1760–1763.
- (35) Tada, K.; Shimazu, K. Kinetic Studies of Reduction of Nitrate Ions at Sn-modified Pt Electrodes using a Quartz Crystal Microbalance. *J. Electroanal. Chem.* **2005**, *577*, 303–309.
- (36) Yang, J.; Duca, M.; Schouten, K. J. P.; Koper, M. T. Formation of Volatile Products during Nitrate Reduction on a Sn-modified Pt Electrode in Acid Solution. *J. Electroanal. Chem.* **2011**, *662*, 87–92.
- (37) Molodkina, E.; Botryakova, I.; Danilov, A.; Souza-Garcia, J.; Feliu, J. Mechanism of Nitrate Electroreduction on Pt (100). *Russ. J. Electrochem.* **2012**, *48*, 302–315.
- (38) Chen, T.; Li, H.; Ma, H.; Koper, M. T. Surface Modification of Pt (100) for Electrocatalytic Nitrate Reduction to Dinitrogen in Alkaline Solution. *Langmuir* **2015**, *31*, 3277–3281.
- (39) Molodkina, E. B.; Botryakova, I.; Danilov, A.; Souza-Garcia, J.; Feliu, J. M. Kinetics and Mechanism of Nitrate and Nitrite Electroreduction on Pt (100) Electrodes Modified by Copper Adatoms. *Russ. J. Electrochem.* **2013**, *49*, 285–293.
- (40) Katsounaros, I.; Figueiredo, M. C.; Chen, X.; Calle-Vallejo, F.; Koper, M. T. Structure- and Coverage-Sensitive Mechanism of NO Reduction on Platinum Electrodes. *ACS Catal.* **2017**, *7*, 4660–4667.
- (41) Kato, M.; Okui, M.; Taguchi, S.; Yagi, I. Electrocatalytic Nitrate Reduction on Well-defined Surfaces of Tin-modified Platinum, Palladium and Platinum–Palladium Single Crystalline Electrodes in Acidic and Neutral Media. *J. Electroanal. Chem.* **2017**, *800*, 46–53.
- (42) Schmidt, T. J.; Markovic, N.; Stamenkovic, V.; Ross, P.; Attard, G.; Watson, D. Surface Characterization and Electrochemical Behavior of Well-Defined Pt–Pd {111} Single-Crystal Surfaces: A Comparative Study Using Pt {111} and Palladium-Modified Pt {111} Electrodes. *Langmuir* **2002**, *18*, 6969–6975.
- (43) Jin, M.; Liu, H.; Zhang, H.; Xie, Z.; Liu, J.; Xia, Y. Synthesis of Pd Nanocrystals Enclosed by {100} Facets and with Sizes < 10 nm for Application in CO oxidation. *Nano Res.* **2011**, *4*, 83–91.

- (44) Xie, X.; Gao, G.; Pan, Z.; Wang, T.; Meng, X.; Cai, L. Large-Scale Synthesis of Palladium Concave Nanocubes with High-Index Facets for Sustainable Enhanced Catalytic Performance. *Sci. Rep.* **2015**, *5*, No. 8515.
- (45) Xia, X.; Xie, S.; Liu, M.; Peng, H.-C.; Lu, N.; Wang, J.; Kim, M. J.; Xia, Y. On the Role of Surface Diffusion in Determining the Shape or Morphology of Noble-Metal Nanocrystals. *Proc. Natl. Acad. Sci. U.S.A.* **2013**, *110*, 6669–6673.
- (46) Zhu, C.; Zeng, J.; Tao, J.; Johnson, M. C.; Schmidt-Krey, I.; Blubaugh, L.; Zhu, Y.; Gu, Z.; Xia, Y. Kinetically Controlled Overgrowth of Ag or Au on Pd Nanocrystal Seeds: From Hybrid Dimers to Nonconcentric and Concentric Bimetallic Nanocrystals. *J. Am. Chem. Soc.* **2012**, *134*, 15822–15831.
- (47) Wang, Y.; Zhou, W.; Jia, R.; Yu, Y.; Zhang, B. Unveiling the Activity Origin of a Copper-based Electrocatalyst for Selective Nitrate Reduction to Ammonia. *Angew. Chem.* **2020**, *132*, 5388–5392.
- (48) Shi, M.-M.; Bao, D.; Wulan, B. R.; Li, Y. H.; Zhang, Y. F.; Yan, J. M.; Jiang, Q. Au Sub-Nanoclusters on TiO₂ toward Highly Efficient and Selective Electrocatalyst for N₂ Conversion to NH₃ at Ambient Conditions. *Adv. Mater.* **2017**, *29*, No. 16065.
- (49) Kresse, G.; Furthmüller, J. Efficient Iterative Schemes for Ab Initio Total-Energy Calculations using a Plane-Wave Basis Set. *Phys. Rev. B* **1996**, *54*, 11169.
- (50) Blöchl, P. E. Projector Augmented-Wave Method. *Phys. Rev. B* **1994**, *50*, 17953.
- (51) Kresse, G.; Joubert, D. From Ultrasoft Pseudopotentials to the Projector Augmented-Wave Method. *Phys. Rev. B* **1999**, *59*, 1758.
- (52) Perdew, J. P.; Burke, K.; Ernzerhof, M. Generalized Gradient Approximation Made Simple. *Phys. Rev. Lett.* **1996**, *77*, 3865.
- (53) Methfessel, M.; Paxton, A. High-precision Sampling for Brillouin-zone Integration in Metals. *Phys. Rev. B* **1989**, *40*, 3616.
- (54) Monkhorst, H. J.; Pack, J. D. Special Points for Brillouin-zone Integrations. *Phys. Rev. B* **1976**, *13*, 5188.
- (55) Mathew, K.; Sundararaman, R.; Letchworth-Weaver, K.; Arias, T.; Hennig, R. G. Implicit Solvation Model for Density-Functional Study of Nanocrystal Surfaces and Reaction Pathways. *J. Chem. Phys.* **2014**, *140*, No. 084106.
- (56) Mathew, K.; Kolluru, V. C.; Mula, S.; Steinmann, S. N.; Hennig, R. G. Implicit Self-Consistent Electrolyte Model in Plane-Wave Density-Functional Theory. *J. Chem. Phys.* **2019**, *151*, No. 234101.
- (57) Grimme, S.; Antony, J.; Ehrlich, S.; Krieg, H. A consistent and Accurate Ab Initio Parametrization of Density Functional Dispersion Correction (DFT-D) for the 94 Elements H-Pu. *J. Chem. Phys.* **2010**, *132*, No. 154104.
- (58) Rumble, J. R.; Lide, D. R.; Bruno, T. J. *CRC Handbook Of Chemistry And Physics*; CRC Press, 2018.
- (59) Henkelman, G.; Uberuaga, B. P.; Jónsson, H. A climbing Image Nudged Elastic Band Method for Finding Saddle Points and Minimum Energy Paths. *J. Chem. Phys.* **2000**, *113*, 9901–9904.
- (60) Henkelman, G.; Jónsson, H. Improved Tangent Estimate in the Nudged Elastic Band Method for Finding Minimum Energy Paths and Saddle Points. *J. Chem. Phys.* **2000**, *113*, 9978–9985.
- (61) Nørskov, J. K.; Rossmeisl, J.; Logadottir, A.; Lindqvist, L.; Kitchin, J. R.; Bligaard, T.; Jónsson, H. Origin of the Overpotential for Oxygen Reduction at a Fuel-Cell Cathode. *J. Phys. Chem. B* **2004**, *108*, 17886–17892.
- (62) Bell, R. The Proton in Chemistry, (Cornell, Ithaca, 1973). In *Tunneling in Biological Systems* Chance, B.; DeVault, D.; Frauenfelder, H.; Schrieffer, J. R.; Sutin, N.; Marcus, R. A., Eds.; Academic Press: New York, 1979; p 729.
- (63) Perrin, D. D. *Ionisation Constants of Inorganic Acids and Bases in Aqueous Solution*; Elsevier, 2016.
- (64) Jin, M.; Zhang, H.; Xie, Z.; Xia, Y. Palladium Concave Nanocubes with High-Index Facets and Their Enhanced Catalytic Properties. *Angew. Chem., Int. Ed.* **2011**, *50*, 7850–7854.
- (65) Wang, L.; Zhai, J.-J.; Jiang, K.; Wang, J.-Q.; Cai, W.-B. Pd–Cu/C Electrocatalysts Synthesized by One-pot Polyol Reduction toward Formic Acid Oxidation: Structural Characterization and Electrocatalytic Performance. *Int. J. Hydrogen Energy* **2015**, *40*, 1726–1734.
- (66) Cerritos, R. C.; Guerra-Balcázar, M.; Ramírez, R. F.; Ledesma-García, J.; Arriaga, L. G. Morphological Effect of Pd Catalyst on Ethanol Electro-Oxidation Reaction. *Materials* **2012**, *5*, 1686–1697.
- (67) Furuya, N.; Yoshida, H. Electroreduction of Nitrous Oxide to Nitrogen Using a Gas-Diffusion Electrode Loaded with Pt Catalyst. *J. Electroanal. Chem. Interfacial Electrochem.* **1991**, *303*, 271–275.
- (68) Reyter, D.; Bélanger, D.; Roué, L. Elaboration of Cu–Pd Films by Coelectrodeposition: Application to Nitrate Electroreduction. *J. Phys. Chem. C* **2009**, *113*, 290–297.
- (69) Reyter, D.; Bélanger, D.; Roué, L. Study of the Electroreduction of Nitrate on Copper in Alkaline Solution. *Electrochim. Acta* **2008**, *53*, 5977–5984.
- (70) Reyter, D.; Bélanger, D.; Roué, L. Elaboration by High-Energy Ball Milling of Copper/Palladium Composite Materials—Characterization and Electrocatalytic Activity for the Reduction of Nitrate in Alkaline Medium. *J. Electroanal. Chem.* **2008**, *622*, 64–72.
- (71) Tacke, T.; Vorlop, K. D. Kinetische Charakterisierung von Katalysatoren zur selektiven Entfernung von Nitrat und Nitrit aus Wasser. *Chem. Ing. Tech.* **1993**, *65*, 1500–1502.
- (72) Li, J.; Zhou, P.; Li, F.; Ma, J.; Liu, Y.; Zhang, X.; Huo, H.; Jin, J.; Ma, J. Shape-Controlled Synthesis of Pd Polyhedron Supported on Polyethyleneimine-Reduced Graphene Oxide for Enhancing the Efficiency of Hydrogen Evolution Reaction. *J. Power Sources* **2016**, *302*, 343–351.
- (73) Clark, C. A.; Reddy, C. P.; Xu, H.; Heck, K. N.; Luo, G.; Senftle, T. P.; Wong, M. S. Mechanistic Insights into pH-Controlled Nitrite Reduction to Ammonia and Hydrazine over Rhodium. *ACS Catal.* **2020**, *10*, 494–509.